

Nanodiamond-Assisted High Performance Lithium and Sodium Ions Co-Storage

Xiaochen Sun, Xuan Gao* , Chang Su, Wei Cheng, Nan Gao, Xin Zhang, Mengmeng Gong, Haobo Dong, Yuhang Dai*, Guanjie He* , and Hongdong Li* 

While lithium resources are scarce for high energy-dense lithium-ion batteries (LIBs), sodium-ion batteries (SIBs), serving as an alternative, inherently suffer from low capacity and the high-cost use of non-graphite anodes. Combining Li- and Na-ions within a single battery system is expected to mitigate the shortcomings of both systems while leveraging their respective advantages. In this study, we developed and assembled a nanodiamonds (NDs)-assisted co-Li/Na-ion battery (ND-LSIB). This innovative battery system comprised a commercial graphite anode, an ND-modified polypropylene (DPP) separator, a hybrid lithium/sodium-based electrolyte, and a cathode. It is theoretically and experimentally demonstrated that the ND/Li co-insertion can serve as an ion-drill opening graphite layers and reconstructing graphite anodes into few-layered graphene with expanding interlayer space, achieving highly efficient Li/Na storage and the theoretical maximum of LiC_6 for Li storage in graphite. In addition, ND is helpful for creating a LiF-/NaF-rich hybrid solid electrolyte interface with improved ionic mobility, mechanical strength, and reversibility. Consequently, ND-LSIBs have higher specific capacities ~ 1.4 times the theoretical value of LIBs and show long-term cycling stability. This study proposes and realizes the concept of Li/Na co-storage in one ion battery with compatible high-performance, cost-effectiveness, and industrial prospects.

1. Introduction

Lithium-ion batteries (LIBs) with high-energy density and long cycling stability have dominated the markets of second-ion batteries. However, scarce crustal lithium (Li) resources and safety problems have hindered the sustainable development of LIBs.^[1] To address this issue,

Dr. X. Sun, Dr. W. Cheng, Prof. N. Gao, Dr. X. Zhang, M. GongMiss, Prof. H. Li
State Key Lab of Superhard Materials, College of Physics, Jilin University,
Changchun 130012, China

E-mail: scx22@jlu.edu.cn

E-mail: hdli@jlu.edu.cn

Dr. X. Gao, Dr. H. Dong, Dr. Y. Dai, Prof. G. He

Christopher Ingold Laboratory, Department of Chemistry, University College
London, 20 Gordon Street, London WC1H 0AJ, UK


E-mail: uccaxga@ucl.ac.uk

E-mail: whutdyh@gmail.com

E-mail: g.he@ucl.ac.uk

Dr. C. Su

Nuffield College, University of Oxford, New Road, Oxford OX1 1NF, UK

 The ORCID identification number(s) for the author(s) of this article can be found under <https://doi.org/10.1002/eam2.12749>.

DOI: 10.1002/eam2.12749

sodium-ion batteries (SIBs) are considered the most promising substitute, as SIBs can use nearly the same production line and rely on the widespread availability of sodium (Na) resources on the earth.^[2] However, SIBs have lower energy density and cycling instability than LIBs due to Na-ion's larger ionic radius and higher equivalent weight.^[3] In addition, cost-effectiveness graphite anodes widely applied in commercial LIBs are not suitable for extraction/insertion of large-sized Na-ions in SIBs.^[4] To improve the capacity and cyclability of SIBs, various carbonaceous materials,^[5] including hard-carbon,^[6] soft-carbon,^[7] anthracite,^[8] expanded graphite (EG),^[9] and graphene,^[10] have been proposed. However, these carbonaceous anode materials are usually produced by complex and/or extreme fabrication processes (e.g., treatments at high temperatures above 2000 °C and/or strong acid-alkali), which would lead to serious environmental issues and an increase in production cost.

To overcome these limitations and leverage the advantages of both LIBs and SIBs, combining charged-discharged Li-ions and Na-ions within a co-Li-/Na-ion battery (LSIB) becomes

a promising strategy to improve the overall performances of batteries. Previous studies have introduced Li-free $\text{Na}_3\text{V}_2(\text{PO}_4)_2\text{O}_2\text{F}$ as cathodes in LIBs to increase the working voltage,^[11] or employed metallic Na anodes in LIBs with Li-/Na-based electrolyte and Li cathodes to achieve low-voltage hysteresis and stable cycling performances.^[12] However, these attempts did not show significant improvements in specific capacity, cost-effectiveness, and safety than traditional LIBs or SIBs. Compared with individual LIBs or SIBs, LSIBs require simultaneous modulation of the components of electrodes, electrolytes, and separators, which is a challenging task as it is difficult to meet all the demands for high-reversible capacity, charge-discharge cycling stability, and cost-effectiveness, meanwhile ensuring compatibility with the production lines of LIBs. Therefore, it is imperative to put forward a state-of-the-art material that strongly interacts with both Li-ions and Na-ions, combining their advantages in one battery system.

In recent years, nanodiamonds have been widely used in energy storage devices because of their high surface area, good mechanical properties, abundant and controllable surface functional groups, high-chemical stability, and powerful Li- and Na-ion adsorption properties.^[13–15] In this study, we design an ND-assisted LSIB (ND-LSIB) that is assembled with a conventional commercial graphite anode,

mixed Li-/Na-electrolyte, polypropylene (PP) separator, and a Li-Na alloy counter electrode for half-cells or the carbon-supported $\text{Li}_{1.5}\text{Na}_{1.5}\text{V}_2(\text{PO}_4)_3$ (LNVP-C) cathode for full-cells, both ND-LSIB half-cells and full-cells exhibit favorable long-term cycling stability and specific capacities of 456 mA h g^{-1} and 121 mA h g^{-1} , respectively, which higher than the case of LIBs. Experimental observation and theoretical simulation reveal that ND combined with Li-ions can serve as an ion drill to open the graphite layers and reconstruct the graphite anode into few-layer graphene (FLG) during the charging and discharging processes, which serves as an enhanced Li/Na storage unit by forming ND@Li/Na core-shell structure. In addition, the LiF-/NaF-rich hybrid solid electrolyte interface (SEI) was created with the assistance of ND, enabling LSIBs with excellent ionic conductivity and mechanical strength. All of these findings are greatly helpful in improving the electrochemical performance of second-ion batteries and can lead to further industrial applications.

2. Results and Discussion

2.1. Optimization Strategy and Assembly of LSIBs

Most battery materials today are synthesized from precursors, primarily lithium carbonate (Li_2CO_3) and sodium carbonate (Na_2CO_3). Fluctuations in the prices of these raw materials can have significant implications for battery cell costs per GWh. Na_2CO_3 prices are approximately two orders of magnitude lower than their lithium counterparts, with Li_2CO_3 at \$27 175 per metric ton compared to Na_2CO_3 at \$239 per metric ton in October 2023. Furthermore, the price trends for these materials differ significantly. Since 2010, the price of lithium carbonate has surged from \$5180 to \$27 175 per metric ton (a 425% increase), while Na_2CO_3 has seen a more modest increase from \$128 to \$239 per metric ton (an 86% rise).^[16] The widespread availability of sodium, coupled with a mature soda ash mining industry, ensures the stability of Na_2CO_3 prices for the foreseeable future. The advantages of the strategy of LSIBs can be simply expressed by the following formula while keeping the same medium voltage,

Raw material cost savings(%)

$$= 1 - \frac{[C_{\text{Li}_2\text{CO}_3} \cdot (1-x) + C_{\text{Na}_2\text{CO}_3} \cdot x] + y}{C_{\text{Li}_2\text{CO}_3} + y}, \quad (1)$$

where the proportion of Na-based raw materials is x , and other raw material costs is y . $C_{\text{Li}_2\text{CO}_3}$ is the cost of Li_2CO_3 , while $C_{\text{Na}_2\text{CO}_3}$ is the cost of Na_2CO_3 .

The strategy in this work is shown in **Figure 1**. In an LSIB full-cell, 50 molar % of Li in the cathode and electrolyte is replaced by Na to realize the collaborative transport and storage of Li-/Na-ions, and the traditional graphite for LIBs is still serving as anode for LSIB, which is reconstructed into few-layered graphene by the migration of ND@Li ion-drill during the charge and discharge processes, which provides a broader path for Na-ions' migration and adsorption. The storage mechanism of Li-ions intercalate into graphite layers while Na-ions adsorbed on FLG interlayer surface enables LSIBs with similar median voltage to LIBs. Furthermore, the quantity of NDs employed in a single LSIB is minimal, approximately three micrograms, constituting merely about 1% of the overall cost of the cell. This indicates that the cost of introducing NDs is meager. 1 GWh battery system requires about 2500 tons of lithium iron phosphate (LFP) cathode material and about 1400 tons of electrolyte. One ton of Li_2CO_3 can produce 32 tons of electrolyte or 4 tons of LFP cathode material. Therefore, 1 GWh LFP battery requires Li_2CO_3 raw materials with a value of ~\$18 173 281. In this work, 50% of Li is replaced with Na, which is expected to save more than \$9 000 000 per GWh in the LFP battery system.

The LSIB half-cells consisted of the commercial graphite anode, PP separator generally used in LIBs, mixed electrolytes of LiPF_6 (for LIBs) and NaPF_6 (for SIBs) in an ethylene carbonate/dimethyl carbonate solution, and Li-Na alloys counter electrode with various mass ratios of Li and Na. As shown in **Figure S2a**, Supporting information, the Li-Na alloys were prepared by a mechanical compression method. After multiple folding (at least six times) and compressing processes, the color of alloy products changed gradually from gold to silvery (**Figure S2b**, Supporting information), representing the complete mixing of Li and Na metals. The symmetric cells taking Li-Na alloy as the counter electrodes (**Figure S2c**, Supporting information) have better long-term cycling

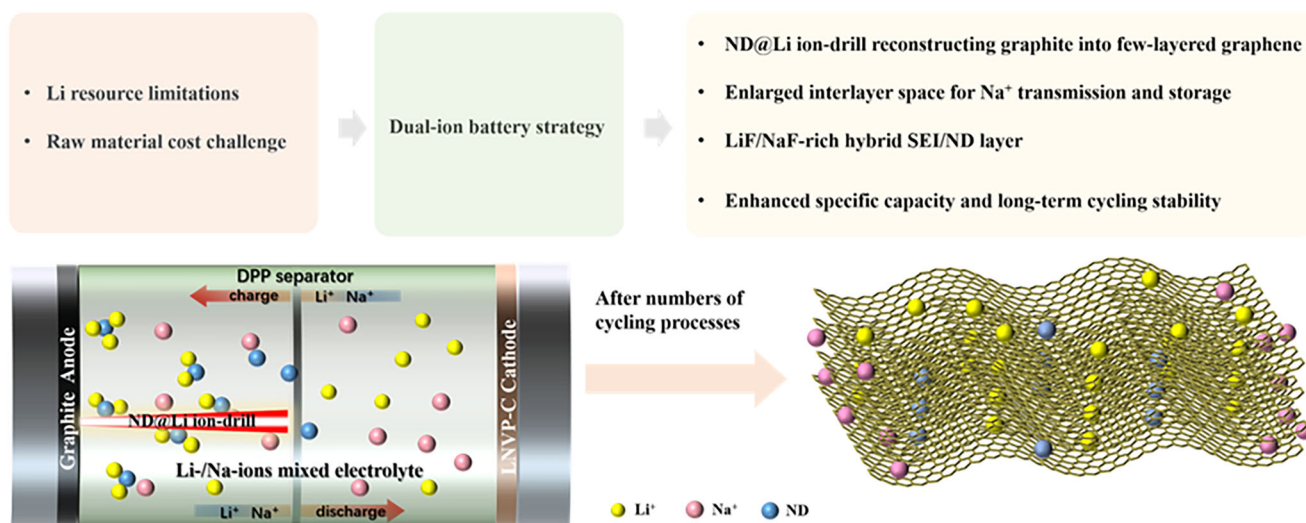


Figure 1. Schematic illustration for the components and working mechanism of ND-LSIBs.

stability than Li//Li (Figure S2c, Supporting information) or Na//Na (Figure S2d, Supporting information) symmetric cells because the intrinsic electrostatic repulsion between Li-ions and Na-ions can lead to a flat ions deposition on the surface of metal electrodes, which further reacts with electrolytes forming an artificial Li-/Na-related SEI,^[12] and the dendrites growth due to the higher reduction potential of alone Na-ions or Li-ions can be will restrained^[17] (Figure S2f, Supporting information).

After examining the electrochemical properties of the LSIBs with varying assemblies (Figures S3–S5, Supporting information), the Li–Na alloy with the mass ratio of 1: 2, Li-/Na-ion mixed electrolyte (equivalent LiPF₆ and NaPF₆ with a volume ratio of 1:1), as well as the PP separator, are optimized to realize high-performance LSIBs. As expected, the specific capacities of LSIBs were lower than LIBs but higher than SIBs, due to the compensation of the co-storage behaviors of Li and Na during charge–discharge processes, especially when using graphitic as the anode material. To boost the performance of LSIBs, we intentionally introduced detonation NDs having favorable chemical inertness, large specific surface area, high-mechanical properties, and ion absorption^[13,18] into LSIBs (named as ND–LSIBs), as described in Figure S5, Supporting information, and the experimental section. The results indicate that the ND-modified PP separator (DPP) can

significantly improve the specific capacity and cycling stability of LSIB. In addition, it is reported that the rigid Li- and Na-related SEI tends to crack during long-term cycles,^[19] and introducing NDs can effectively fill the crack (Figure S2e,g, Supporting information) and improve the plating/stripping performance of Li, Na, and alloy Li–Na symmetric cells, because of the lower nucleation potential for alkali metals, beneficial size-effect, and mechanical properties of NDs. Therefore, the Li-/Na co-deposition has better stability than the case of Li or Na alone, and the ND can further enhance the advantages of Li–Na co-storage battery systems, which laid the foundation for the Li–Na alloy used as reference electrode or metal anode in LSIB half-cells.

2.2. The Li/Na Co-Storage Performance in LSIB Half-Cells with Graphite Anode

The LSIBs were assembled according to the optimized conditions. The CV curves were tested at various scan rates from 0.1 to 1.0 mV s⁻¹, revealing the electrochemical kinetics mechanism of the graphite anode in both LSIBs (Figure 2a) and ND–LSIBs (Figure 2b). During the first few cycles, although the curve features are similar, the peak areas of ND–LSIBs (Figure S6d, Supporting information) are close to the case of

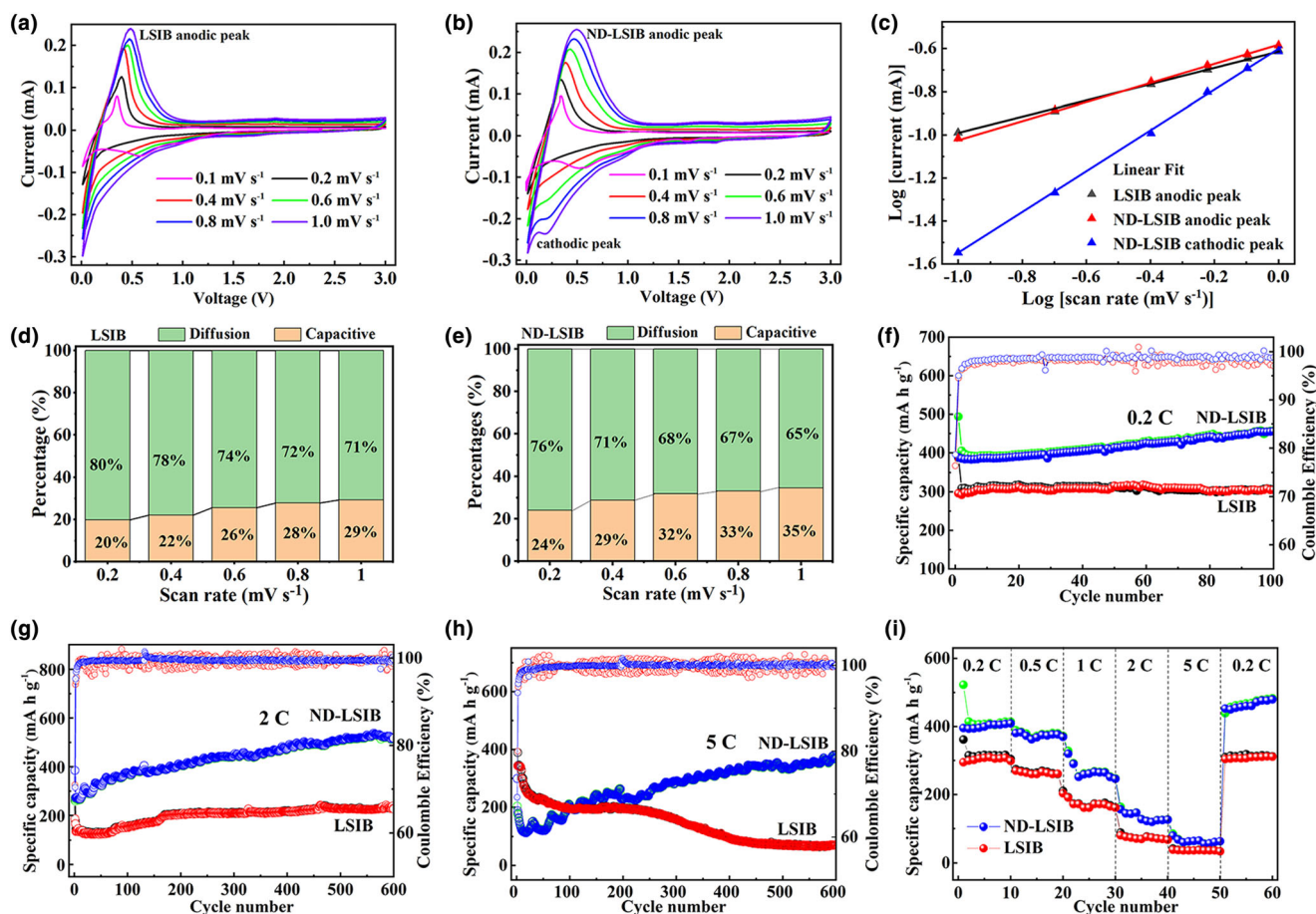


Figure 2. The CV curves of a) LSIB and b) ND–LSIB half-cells tested between 0.01 V and 3.00 V at different scan rates of 0.1–1.0 mV s⁻¹. c) The plot of log (scan rate) versus log (peak current) calculated from CV curves of LSIB and ND–LSIB. Trends of the capacitive contribution of d) LSIB and e) ND–LSIB at different sweep rates of 0.2–1.0 mV s⁻¹. Cycle performances of LSIB and ND–LSIB half-cells at rates of f) 0.2 C, g) 2 C, and h) 5 C. i) Rate performances at various current densities.

LIBs, and significantly larger than those of LSIBs (Figure S6c, Supporting information) or SIBs, indicating that introducing NDs is favorable for decreasing impedance and increasing the diffusion coefficient of the cells.^[20] This is further supported by electrochemical impedance spectroscopy (EIS) results (Figures S7, S8, and Table S1, Supporting information). In addition, the CV curves of ND–LSIBs have incorporated the characteristic peaks of both LIBs and SIBs, and the large impedance and poor transfer kinetics of SIBs relating to the heavy atomic mass and larger ionic radius of Na have been well relieved. The area enclosed by the CV curve represents the overall capacity, which can be identified in the diffusion and surface control processes.^[21] The current intensity (i) as a function of scan rate (v) is plotted in Figure 2c following a power-law formula of $i = av^b$, the constants a and b in the equation are related to the reaction behavior, where a slope value (indicative of b) of 1.0 corresponds to a surface-controlled process (capacitor behavior), while a value of 0.5 corresponds to a diffusion-controlled process (diffusion behavior).^[21,22] In both LSIB and ND–LSIB cells, the typical diffusion-controlled process of ions dominates in the graphitic anodes. In addition, NDs prefer the surface-controlled process (pseudo-capacitor contribution) for increasing the storage of Li- and Na-ions compared to LSIBs, as analyzed in Figure 2d,e.

The increasing storage can be attributed to the strong covalent C–C bonds of NDs, which have a short bond length of 1.54 Å and an inter-spacing of (111) plane of ~ 2.06 Å,^[23] making the surface of ND particles energetically favorable for absorption of Li- and Na-ions (as calculated in Figure S9, Supporting information), rather than their diffusion and/or intercalate inside the NDs. After charge–discharge cycling processes, the charge-transfer and interface layer resistance of ND–LSIBs are significantly lower than those of LSIBs, as examined by EIS spectra. This, combined with the enhanced transfer kinetic, indicates that the NDs could activate the graphite anode, providing a more efficient route for the migration and storage of Li-/Na-ions.

In Figure 2f, the LSIB half-cell exhibits a specific capacity of 304 mA h g^{-1} after 100 charge–discharge cycling processes at a rate of 0.2 C ($1 \text{ C} = 372 \text{ mA h g}^{-1}$), which is significantly higher than the capacity of SIBs with the same graphite anode (24 mA h g^{-1}) but lower than that of LIBs ($\sim 376 \text{ mA h g}^{-1}$), as shown in Figure S10, Supporting information. The ND–SIB shows a specific capacity of $\sim 90 \text{ mA h g}^{-1}$, which is significantly higher than that of SIB, indicating that ND can absorb Na-ions providing some capacity. The different capacities of the graphite anode for the two types of ions should come from the large-sized Na-ions hindering the intercalation reaction of Li-ions in the graphite anode, leading to a decreased reversible capacity. The initial Coulombic efficiencies (CEs) of LSIBs and ND–LSIBs are $\sim 76\%$ and $\sim 79\%$ (Figure S11a,b, Supporting information), respectively, closely related to the formation of SEI layers during the first discharging process. Both CEs are above 98% after several cycles, indicating high charge–discharge effectivity and good cycling stability. In Figure S11c, Supporting information, both LSIB and ND–LSIB have a high capacity contribution of above 80% in the platform region of electrochemical curves at 0–0.8 V, corresponding to a multi-step lithiation and sodiation processes with the formation of a series of Li-GICs and Na-graphite compounds for energy storage.^[24,25] The slope region capacity of above 0.8 V is contributed by the adsorption of Li-/Na-ions on the active sites of the graphite anode. Interestingly, for the case of ND–LSIB, the reversible capacity smoothly increases from the initial 400 mA h g^{-1} at the 2nd cycle to 456 mA h g^{-1} at the 100th cycle performed at 0.2 C, which is higher than that of LSIBs and/or the theoretical capacity of LIBs (372 mA h g^{-1}). In contrast, the LSIB maintains

low capacities ($\sim 300 \text{ mA h g}^{-1}$ at the 100th cycle) during the cycling processes. Hence, the ND is beneficial to improve the energy density and cycling stability of LSIB.

When performed at high rates (i.e., 2 C in Figure 2g and 5 C in Figure 2h), the LSIBs exhibit low and rapidly decreasing capacities due to the uncontrolled Na-ions deposition and/or electrode structural damage (Figure S12, Supporting information), similar to conventional SIBs using graphite anodes.^[25] In contrast, the capacities of ND–LSIBs have a rising trend with cycling processes, which is more obvious compared to the case of 0.2 C, this is because when performed at a high current density, a large number of ions can be embedded in the graphite layer in a short time, promoting the embedding of ND and the formation of FLG structure, leading to enhancing active sites for ions storage. After 600 charge–discharge cycles at 2 C and 5 C, the ND–LSIBs exhibit a significantly high reversible capacity of 525 and 361 mA h g^{-1} , respectively, which are ~ 2.4 and 6.2 times higher than those of the LSIB (220 and 58 mA h g^{-1} , respectively), and ~ 1.4 times higher than the theoretical capacity of LIBs at 2 C. In addition, the ND–LSIBs also maintain a CE of $\sim 100\%$, indicating excellent cycling stability, whereas the CE of LSIBs fluctuates largely ($\pm 2\%$). As shown in Figure 2i, when the current density was reduced from 5 C to 0.2 C, the reversible capacity for ND–LSIBs was restored to 460 mA h g^{-1} , with a capacity retention rate of around 115%, significantly higher than those of LSIBs (capacity of 311 mA h g^{-1} and retention rate of 98.8%). These results demonstrate that introducing NDs can dramatically improve the reversibility capacity and cycling stability of LSIBs, especially when performed at high-current density, surpassing even the performance of traditional LIBs.

2.3. The Li/Na Co-Storage Performance and Mechanism in Graphite Anode

It is widely accepted that the electrochemical properties of ion batteries are strongly determined by the characteristics of the anode material and its structure. Upon examining ND–LSIB half-cells after undergoing charge–discharge cycling processes (for example, after 300 cycles at 5 C), it was observed that the initial graphite anode was transformed into an accordion-like FLG structure (Figure 3a) with enlarged interlayer spacing above 4.0 Å (Figure 3b), which provides more favorable transport paths and active sites for the embedding of Li- and/or Na-ions,^[26] this phenomenon is also observed in Figure 3e for ND–LIBs. Note that some ND nanoparticles have migrated from the separator to graphite interlayers, leading to the formation of FLG, and uniform and stable ND–SEI layers are formed between layers (inset in Figure 3a). The content of NDs is mainly dependent on the ND colloid concentration modified on separators, and the amount of NDs used in one LSIB button cell is very small, at approximately $3 \mu\text{g}$. Excessive ND content hinders the dispersion of ND colloid, and the agglomerated ND particles dispersed on the separator will affect the cycle stability and reversibility of batteries, as shown in Figure S13, Supporting information. In contrast, LSIBs without introduced NDs maintain their initial bulk graphite morphology (Figure S12, Supporting information). In addition, FLGs do not appear during the charge–discharge processes of LIBs,^[15] LSIBs, or ND–SIBs (Figure 3i and Figure S12, Supporting information). Therefore, the formation of FLG is a unique result of the combination of NDs with Li-ions (also verified in Figure 3e,f, where a multilayered structure with 20–50 layers is presented clearly), which provides more channels and active sites for the following diffusion and adsorption of

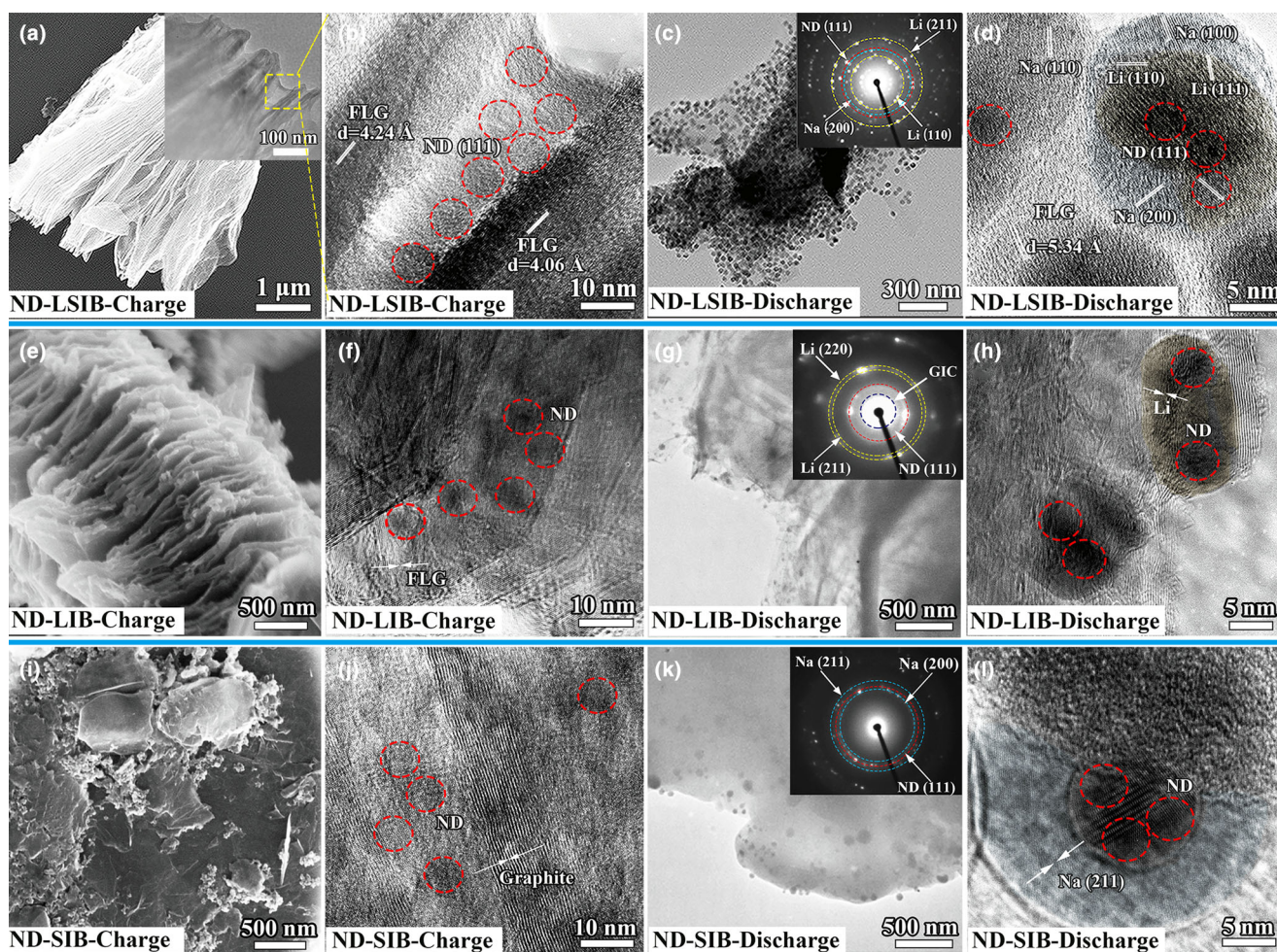


Figure 3. TEM and HRTEM images of the graphitic anodes after 300th charge or discharge in ND-LSIB a–d), ND-LIB e–h), and ND-SIB i–l). The insets in c, g, k) are the corresponding selected-area electron diffraction (SAED) patterns.

Na-ions. In the charge status of the graphite anode in ND-LSIB (Figure 3b), naked detonated ND particles (~ 5 nm in diameter) were observed in the graphite matrix.

Importantly, in the discharge status (Figure 3c), a large number of granular particles with an average diameter of ~ 20 nm were observed, distributing in the graphene matrix at a high density of 2×10^{11} particle cm^{-2} . These granular particles, determined by selected-area electron diffraction (SAED), consist of high crystallinity NDs, metallic Li, and Na. HRTEM images (Figure 3d) evidence that most granules with an average size of ~ 20 nm generally contain 1–4 tiny ND particles, which show a typical core-shell structure comprising of an ND core covered with a thick shell of Li and Na, named as ND@Li/Na. Furthermore, the FLGs show expanding interlayer spacing of ~ 5.3 Å due to the formation of GICs related to the embedding of Li. Since Na cannot form stable GICs when embedded in graphite,^[27] Na-ions are mainly adsorbed on the newly exposed graphite or ND surface to provide capacity. No lithium or Sodium dendrites are observed during charging or discharging statuses, indicating the favorable reversibility of Li- and Na-ions in the ND-assisted graphite anode.

The adsorption and de-adsorption of Li and Na from NDs were reversible and complete during the cycling processes of charge–

discharge, as shown in Figure 3b,d. In the charge processes, the naked ND particles embedded in the hierarchical graphene matrix can create sufficient space for a large number of Li- and Na-ions intercalating in the graphitic anode. Because of the strong electrostatic repulsion between Li-ions and Na-ions,^[19] the Li-ions and Na-ions can independently migrate and phase-separately embed in FLG or attach to one ND core (Figure 3d). The ND@Li/Na particles can be seen as additional nano-receivers of alkali metals in the bulk graphitic anode, resulting in significantly enhanced specific capacity for ND-LSIB cells, as observed in Figure 2f–i. With the high theoretical capacities of 3860 mA h g^{-1} for metallic Li^[28] and 1166 mA h g^{-1} for Na,^[29] the ND@Li/Na units can provide a new Li/Na storage platform in addition to the graphite matrix, further significantly improving the capacity of second ion batteries.

The mechanisms of FLG formation and ion intercalation in graphite anodes associated with NDs are simulated using the CP2K program.^[30] To simplify the simulation, the initial bilayer graphene intercalated with a few Li-ions (LiC_6) having an enlarged interlayer space of ~ 3.7 Å^[31] is proposed to interact with an ND cluster consisting of 75 carbon atoms. When the ND cluster closely approaches the cross-sectional side of the bilayer graphene, charge transfer occurs between the carbon

atoms of the ND surface and graphene layer, and then the ND tends to open and move into the bilayer graphene to a certain depth (the dynamic process is shown in the video image in Attachment 1). When the graphite was opened by an ND particle (Figure 4a), more Li-ions can easily enter into the expanded space, and the repulsion between Li-ions embedded is favorable for further enlarging the layer spacing, which is subsequently beneficial for more NDs entering into the inner of the graphitic anode during repeated charge–discharge cycling processes. Consequently, the thick bulk graphite is stripped into accordion-like FLGs, which will provide more active sites for the combination of Li- and Na-ions, and thus the capacity of the cells could continuously increase along with charge–discharge cycling processes, as observed in Figure 2f–h. Since Na has a large ion diameter and tends to form NaC₆₄ graphite intercalation compound, which is thermodynamic instability,^[27] the combination of ND and Na is thus unfavorable for forming FLGs (Figure 3i), in contrast to the case of Li and ND mentioned above. As a result, the ND@Li can serve as an ion drill during cycles, reconstructing graphite anodes into few-layered graphene (FLG), providing highly efficient Li/Na co-storages, as shown in the schematic illustration of Figure 4c.

In-situ XRD patterns were employed to examine the ion intercalation and de-intercalation statuses in the interlayer of the graphite anode. The intercalation is indicated by spacing expansion, such as the shift of the intrinsic (002) graphite diffraction peak at $2\theta \sim 26.0^\circ$. For the ND–LSIB half-cell (Figure 5a), a series of staging phases are collected with varying applied voltage during the cycling processes. The lithiation begins after the formation of SEI at a higher voltage above 0.65 V. With increasing the discharge time (decreasing voltage) in one circle, the interlayer spacing expansion continuously occurs in the region I with two parts, the one for the evolution process from LiC₂₄ to LiC₁₂ (0.198–0.110 V) and the latter from LiC₁₂ to LiC₆ (0.110–0.065 V). Finally, LiC₆ is formed entirely in the voltage region II of 0.065–

0.010 V with the typical graphite lattice expansion ($2\theta \sim 24.7^\circ$).^[32] The expansion is kept during the continuous discharge process, meaning that at this stage, the further increased capacity is mainly related to the Li-ion absorption on NDs (as shown in Figure 3) at lower applied voltages. Interestingly, in the early stage of the charging process, the desorption of Li-ions from NDs occurs firstly in region III (here, the lattice expansion related to LiC₆ is kept), followed by a fast de-intercalation of Li in the graphite interlayer spacing in the region IV including LiC₁₂, LiC₂₄, and LiC₃₀, etc., and then one charge process is finished.

Figure 5b shows the in-situ XRD patterns of discharging LSIB half-cells without NDs. It is found that the Li intercalation is dominantly associated with the formation of mixed phases of LiC_x ($x > 6$), with nearly few LiC₆ formed. On the contrary, LiC₆ is formed entirely in the same voltage region II of ND–LSIBs (Figure 5a). The difference can explain the lower specific capacity of LSIBs compared to ND–LSIBs (as shown in Figure 2). To understand the specificity of ND enhancements, the in-situ XRD spectra of ND–SIB and ND–LIB are compared. The lattice expansion of the graphite anode does not occur for SIB cells, as most large-sized Na-ions tend to absorb on the surface of graphite rather than intercalating into interlayers, however, the SIB has a broader peak than ND–SIBs (Figure 5c,d), indicating that the graphite anode in ND–SIB is more arranged with higher crystallinity, which proves that ND has partly intercalated into graphite edges. The insertion of ND and its supported graphite layer can both provide pseudocapacitance for overall capacity, lead to a higher Na-ion storage activity. In contrast, assisted with introducing NDs in the LIB cells, the GICs are nearly all LiC₆ (Figure 5e), similar to the ND–LSIB feature. While without ND assistance (Figure 5f), the mixed GICs with the majority of LiC_x ($x > 6$) are presented in LIBs during the cycling process, resulting in less capacity with respect to the case of ND–LIBs.

The in-situ XRD results strongly demonstrate that introducing ND plays a crucial role in improving the performances of LSIB by forming LiC₆ GIC in FLG and ND@Li/Na structure, and the interlayer supporting function of ND can promote the reversibility of Li-ions de/intercalations and enhance Li-/Na-ions co-storage in ND–LSIB system. The chemical diffusion coefficients of Li-/Na-ion ($D_{\text{Li/Na-ion}}$) in graphite anodes are calculated from the GITT discharge curve (Figure 5g,h) versus cell voltage, following Fick's second law of diffusion:^[33]

$$D_{\text{Li}^+} = \frac{4}{\pi} \left(\frac{m_B V_m}{M_B S} \right)^2 \left(\frac{\Delta E_s}{\Delta E_\tau} \right)^2 (\tau L^2 / D_{\text{GITT}}), \quad (2)$$

where m_B , V_m , M_B , S , and L are the mass, molar volume, molecular weight, active surface area and characteristic length in turn. ΔE_s is the change of steady-state voltage of cell for the step in different potential range and ΔE_τ is the total change of cell voltage during the current pulse for the time τ .^[34] The Li-/Na-ion synergistic diffusion coefficient of graphite anode in ND–LSIB (10^{-8} to $10^{-10} \text{ cm}^2 \text{ s}^{-1}$) is higher than the case of LSIB (10^{-9} – $10^{-11} \text{ cm}^2 \text{ s}^{-1}$), revealing the enhanced transfer kinetic of Li-/Na-ions in the ND-supporting graphite layers. The same conclusion is also obtained when the LSIB

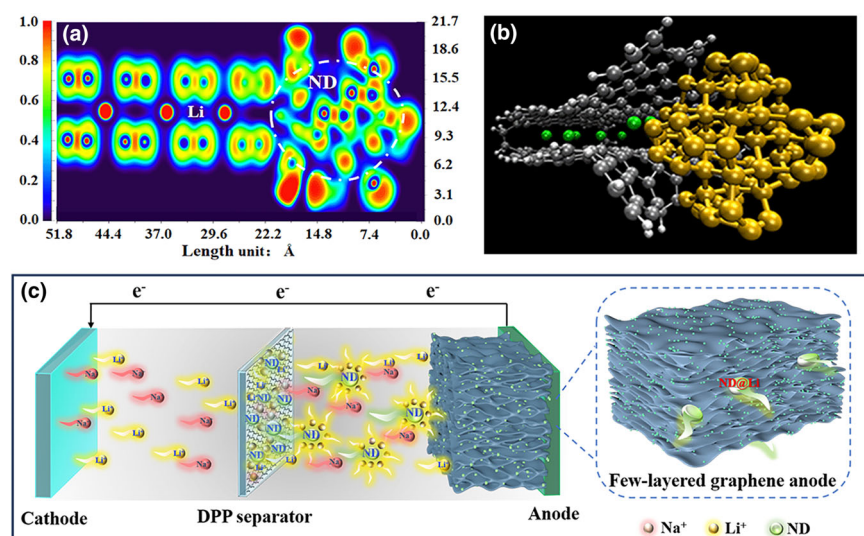


Figure 4. a) Electron localization function (ELF) analysis of electronic structure of the system consisting of bilayer graphene (BLG) with embedded Li-ions and an inserting ND cluster (the color-coded area from blue to red represents the increase in the electronic locality). b) Snapshot of molecular dynamics during intercalation of ND and opening BLG with embedded Li ions, the yellow, green, gray, and white spheres represent the C atoms in ND, Li atoms, C atoms in BLG, and H atoms, respectively. c) Schematic illustration of the structural evolution mechanism of graphite anode during cycles.

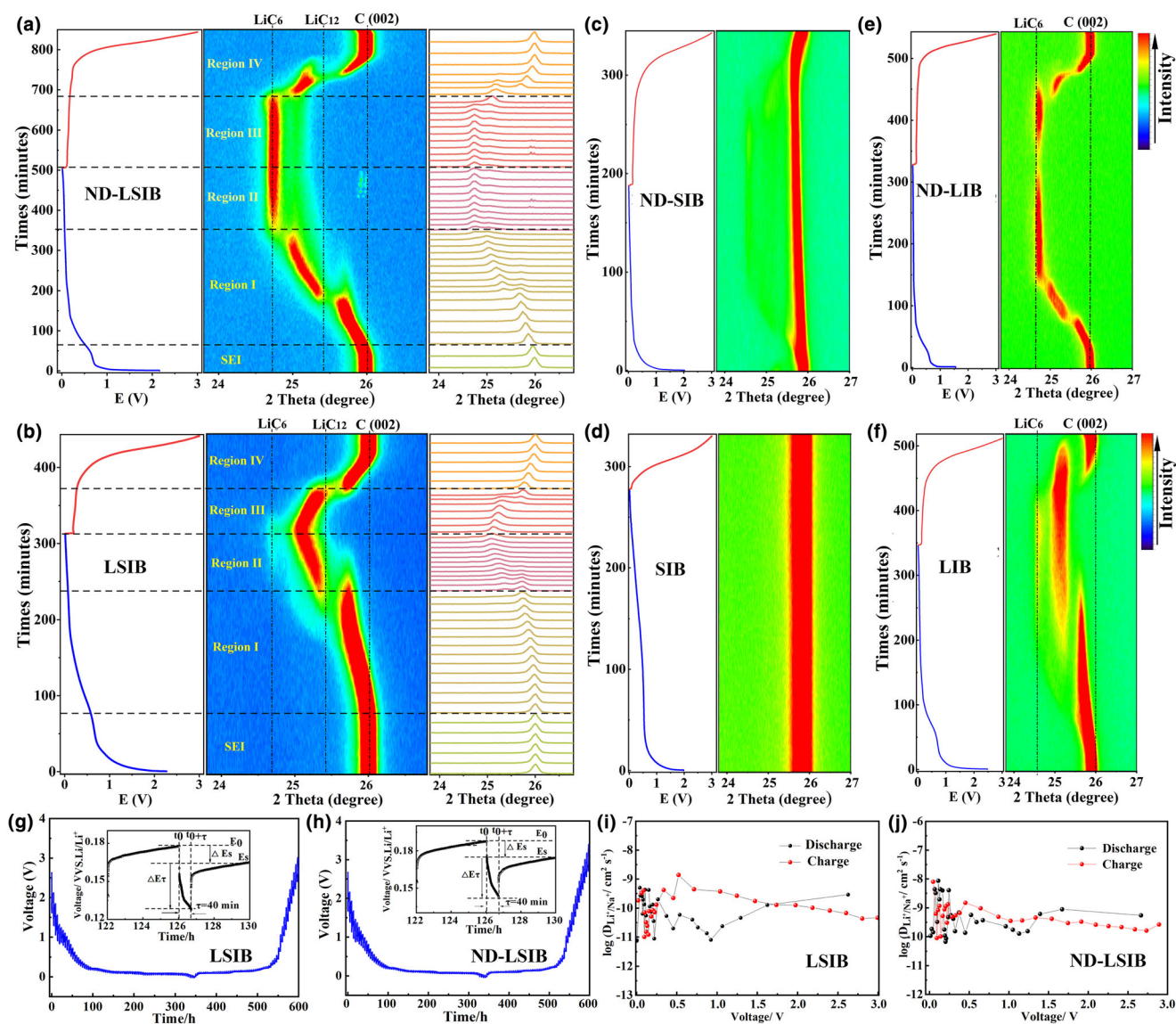


Figure 5. Charge–discharge curves (left) and *in-situ* XRD patterns (middle and/or right) of the graphite anode recorded during the cycling process at a rate of 0.2 C in a) ND–LSIB, b) LSIB, c) ND–SIB, d) SIB, e) ND–LIB, and f) LIB. Discharge–Charge GITT curves of g) LSIB, and h) ND–LSIB as a function of time in the voltage range of 3.00–0.01 V. Insets show a single GITT curve during discharge process. The calculated chemical diffusion coefficients of Li-/Na-ions from the GITT curve in the single-phase regions of i) LSIB, and j) ND–LSIB.

and ND–LSIB cells are cycling at a high rate of 2 C, as shown in Figure S14, Supporting information, suggesting that the crucial role of NDs is also presented for the fast charge and discharge processes. All these *in-situ* XRD results are strongly associated with the electrochemical properties and structural revolutions of the ND–LSIB, LSIB, LIB, and SIB cells.

The measurement of X-ray photoelectron spectroscopy (XPS) was performed on the graphite anode with formed SEI on the surface after cycling processes, confirming that both Li-ions and Na-ions have been involved in the redox reaction contributing to the capacities of cells. The C 1s (Figure 6a) and O 1s spectra (Figure 6b) of hybrid SEI show abundantly $\text{Na}_2\text{CO}_3/\text{Li}_2\text{CO}_3$ and $\text{ROCO}_2\text{Li}/\text{ROCO}_2\text{Na}$ originating from the electrolyte decomposition. An additional peak at ~ 283.6 eV for

ND–LSIB is observed, corresponding to the C–H band^[35] related to the existence of NDs in the SEI layer. The spectra of F 1s (Figure 6c), P 1s (Figure 6d), Li 1s (Figure 6e), and Na 1s (Figure 6f) of the SEI reveal enriched Li/Na hybrid fluorides, such as $\text{Li}_x\text{PF}_y/\text{Na}_x\text{PF}_y$, $\text{Na}_x\text{PO}_y\text{F}_z/\text{Li}_x\text{PO}_y\text{F}_z$, and LiF/NaF species in the SEI for both ND–LSIB and LSIB. The SEI having rich Li- and Na-fluoride species can efficiently reduce the initial side reaction, enhance the ionic conductivity, and improve the mechanical strength compared with the SEI with only Li- or Na-based species.^[35,36] Noted that the contents of LiF and NaF significantly increase in the case of ND–LSIB (Figure 6c,e,f), suggesting that the NDs are favorable for enhancing decomposition and hydrolysis of LiPF_6 salt, which are helpful for further improving the long-term cycling performance of the ND–LSIB.

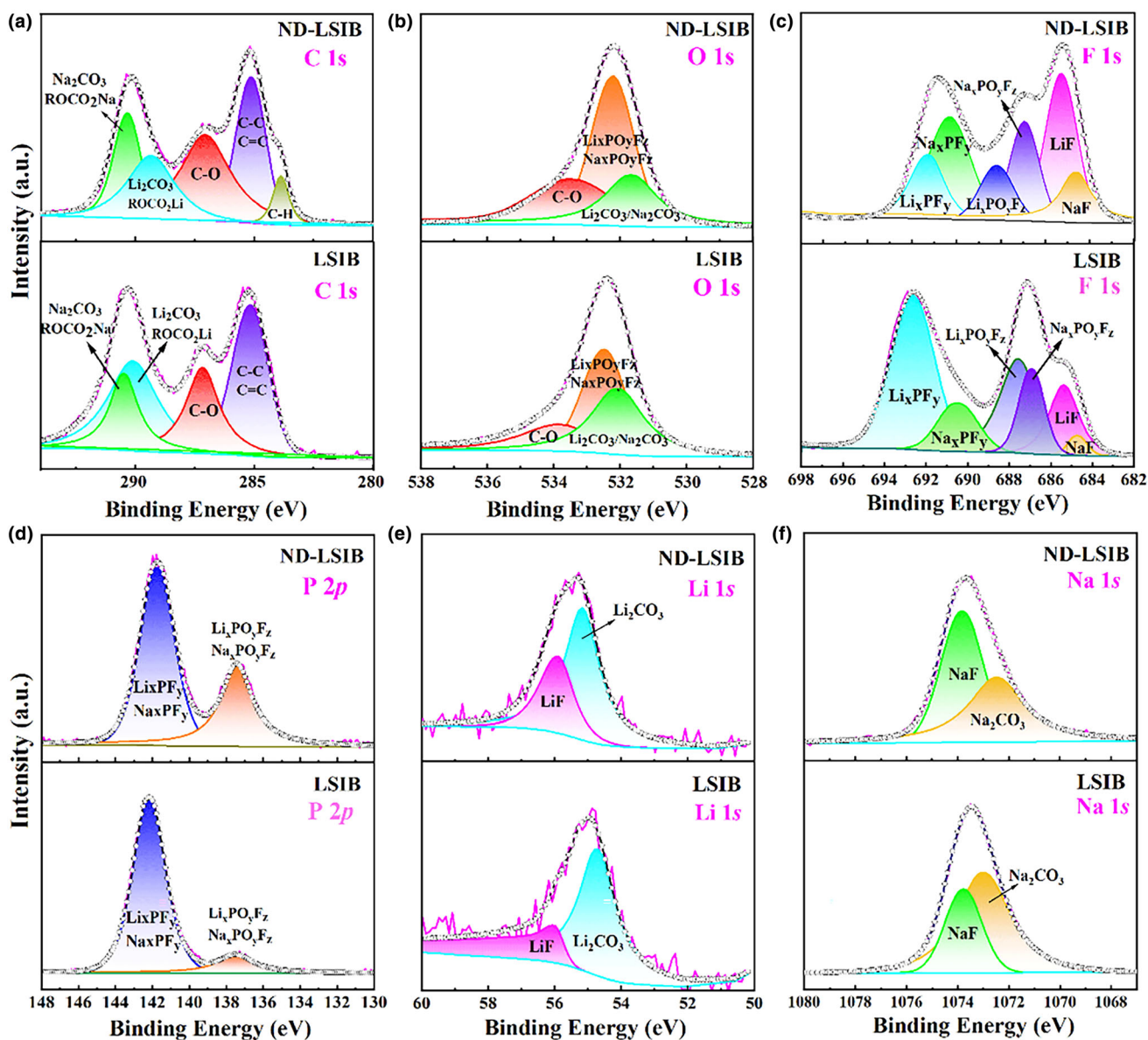


Figure 6. High-resolution XPS spectra of SEI on graphitic anode after the 20th charge–discharge at a rate of 2 C for ND–LSIB and LSIB half-cells. a) C 1s, b) O 1s, c) F 1s, d) P 2p, e) Li 1s, and f) Na 1s.

In addition, the AFM images of graphite anodes after 300 cycles of charges–discharges at a high rate of 5 C reveal a relatively flat surface of graphite anode in ND–LSIB (Figure S15a, Supporting information), which is consistent with TEM results in Figure 3a,b, revealing the excellent mechanical strength and reversibility of SEI layers. Whereas, the anode of LSIB exhibits a rough and uneven surface after cycles, attributed to the continuous decomposition of SEI and the resultant structural damage of graphite (Figures S12 and S15b, Supporting information). As a result, the abundant ND–related Li/Na fluoride species in SEI near the surface of the graphitic anode are thermodynamically stable and serve as a critical factor in stabilizing the SEI layer for positively influencing battery performances.

2.4. Electrochemical Performances of LSIB Full-Cell

To further explore the practicability of graphite anode in ND–LSIBs, a hybrid phase $\text{Li}_{1.5}\text{Na}_{1.5}\text{V}_2(\text{PO}_4)_3\text{-C}$ (LNVP-C) cathode was prepared by a simple modified sol–gel method. The XRD and Raman spectroscopy (Figures S16a,b, Supporting information) are performed, revealing its rhombohedral NASICON structure covered with a microcrystalline carbon layer. The corresponding SEM (Figure S16c, Supporting information) and TEM (Figure S16d, Supporting information) images show a three-dimensional (3D) carbon network structure, which leads to a higher ion and electron mobility, and the corresponding lattice fringe in HRTEM (Figure S16e, Supporting information) is related to the LNVP crystal, connecting to each other and embedded in the 3D carbon

network microcrystalline layer. The electrochemical performances of the LSIB half-cell consisting of LNPV-C cathode and Li–Na counter electrodes were tested between 2.8 and 4.4 V. The LNPV cathode exhibits a high plateau at ~ 3.8 V corresponding to the redox of Li-/Na-ions (Figure S17a,b, Supporting information), after 100 (600) cycles at a current density of 0.1 mA g^{-1} (1 A g^{-1}) (Figure S17c,d, Supporting information), the reversible capacities of 116 mA h g^{-1} (58 mA g^{-1}) for LSIB and 140 mA h g^{-1} (94 mA g^{-1}) for ND–LSIB were recorded. Both LSIB and ND–LSIB exhibit high-rate performance at varying current densities from 0.1 to 2 A g^{-1} (Figure S17e, Supporting information). When the current density was returned to 0.1 A g^{-1} , the reversible capacity is restored to 149 mA h g^{-1} for ND–LSIB and 139 mA h g^{-1} for LSIB, respectively, corresponding to 98% and 89% of the initial reversible capacity.

According to the above half-cell tests, the graphite//LNPV-C LSIBs full-cells were further assembled and measured. In order to enhance the stability and reduce the irreversibility of LSIBs during cycling, all the graphite anodes were chemically prelithiated before assembly. Figure 7a,b are the representative CV profiles of LSIB and ND–LSIB full-cells, respectively, the increased peak intensity and the decreased

potential difference between oxidation/reduction peaks of ND–LSIB indicate that NDs can significantly enhance the electrochemical kinetics and Li-/Na-ions storage capability of graphite electrodes, with respect to the case of LSIB. The GCD curves (Figure 7c) at a current density of 0.1 A g^{-1} indicate that LSIBs with and without NDs possess an average working voltage of ~ 3.6 V in the discharging process. The gap between charge and discharge plateau potentials of ND–LSIB is smaller than that of LSIB, meaning that the ND–LSIB has smaller impedance and larger kinetics, which is further supported by the results of EIS tests (Figure S18, Supporting information).

After 80 cycling processes at a current density of 0.1 A g^{-1} , the capacity of the LSIB full-cell gradually decreases to $\sim 72 \text{ mA h g}^{-1}$ (Figure 7d corresponding to an energy density of $\sim 180 \text{ Wh kg}^{-1}$), originating from the irreversible Na deposition with poor dynamics.^[25] In contrast, the special capacity of the ND–LSIB full-cell is $\sim 121 \text{ mA h g}^{-1}$, corresponding to an energy density of $\sim 300 \text{ Wh kg}^{-1}$, which is nearly equivalent to commercial LIB cells ($250\text{--}350 \text{ Wh kg}^{-1}$)^[37] and great higher than as-reported SIBs ($150\text{--}200 \text{ Wh kg}^{-1}$)^[7,8,25] or Na-compound-cathode-based LIBs ($\sim 230 \text{ Wh kg}^{-1}$).^[11] The ND–LSIB full-cells show a good rate performance (Figure 7e), cycling at increasing

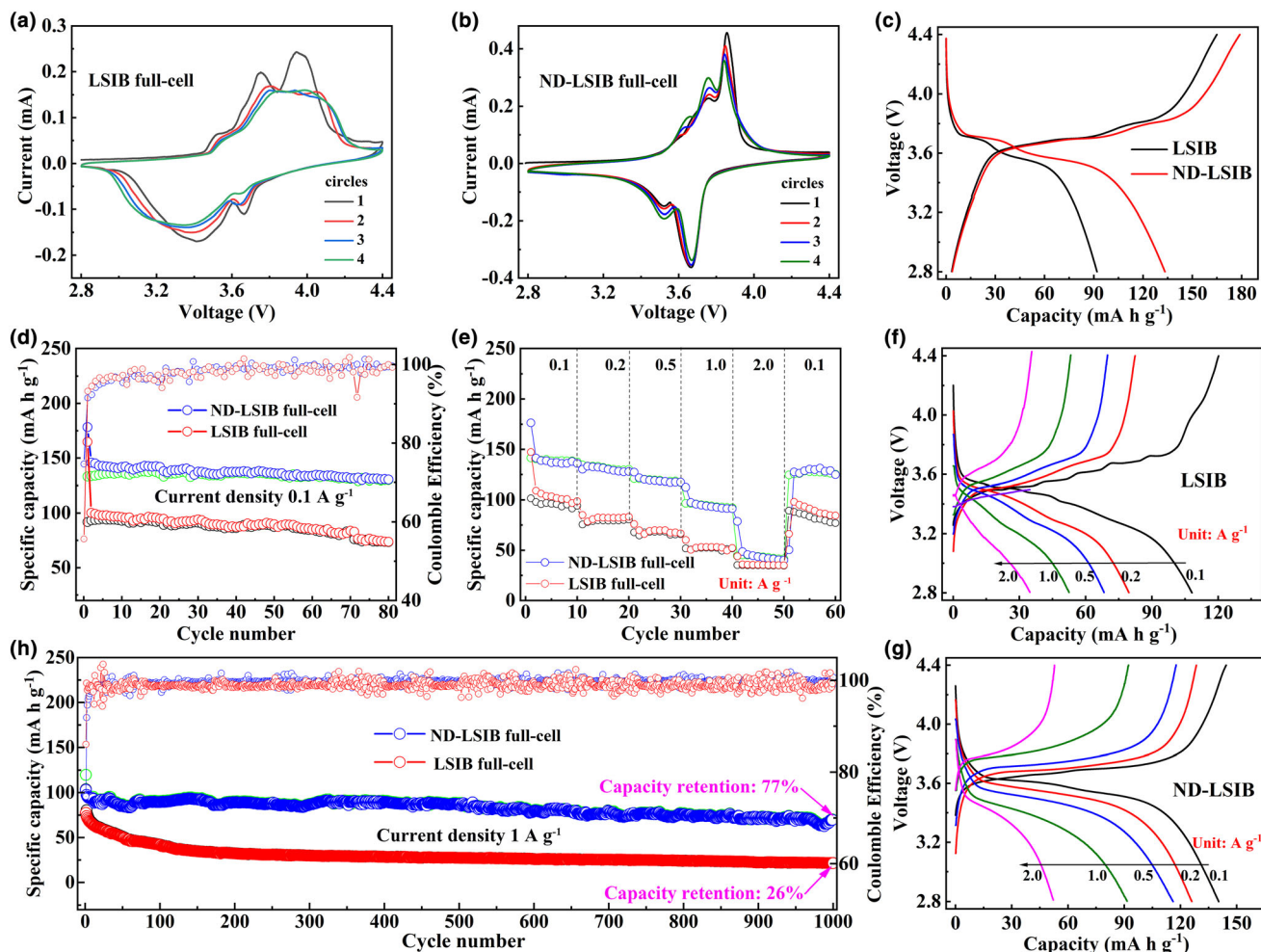


Figure 7. Electrochemical performances of LSIB and ND–LSIB full-cells. a, b) CV curves, c) galvanostatic charging/discharging (GCD) curves and d) cycling performance at a current density of 0.1 A g^{-1} , e) rate performances at various current densities of $0.1\text{--}2 \text{ A g}^{-1}$ and corresponding GCD curves of f) LSIB and g) ND–LSIB. h) Long-term cycling performance at a high current density of 1 A g^{-1} .

current density from 0.1 to 2 A g⁻¹, with corresponding capacity retains of 124 mA h g⁻¹ and capacity retention up to 93.5% when the current density was returned to 0.1 A g⁻¹. On the other hand, the LSIB exhibits poor rate capability and cycling stability, especially at high current densities, with a capacity fading rate as low as 74%. The corresponding GCD curves of LSIB (Figure 7f) indicate that the working voltage suffers from a serious attenuation, resulting in a decreasing energy density. Conversely, ND-LSIB demonstrates a clear discharge plateau above 3.5 V at a high current density of 2.0 A g⁻¹ (Figure 7g), associated with enhanced Li/Na transport kinetics in ND/graphite electrodes.

Significantly, the ND-LSIB full-cell achieves a capacity retention of 77%, with a capacity decay from 91 to 70 mA h g⁻¹ after 1000 cycles at a high current density of 1 A g⁻¹, which was significantly higher than that of LSIB (capacity decay from 81 to 21 mA h g⁻¹) (Figure 7h) and that of assembled LIB full-cell (capacity degradation from 200 to 59 mA h g⁻¹) within 160 cycles (Figure S19, Supporting information). These results indicate that introducing NDs can improve the sluggish kinetics and relief Li and/or Na plating in electrodes during fast charging/discharge processes. Based on the results of ND-LSIB full-cells with and without Na source of Na₃V₂(PO₄)₃ (Figure 7 and Figure S20, Supporting information), the capacity contribution rate of Na-ions in ND-LSIB is estimated to be ~35% when the molar ratio of Li:Na is 1:1 in the cathode, indicating that the abundant active sites of FLG structure and the strong absorption of NDs can significantly improve the Na-ion capacity of graphite anode.

3. Conclusions

In summary, we assemble ND-assisted LSIBs and demonstrate the effectiveness of using NDs to enhance the performance of LSIBs, achieving compatible high performance and low cost in secondary ion batteries. Through comprehensive characterizations and simulations, we have revealed the key role of NDs in improving the performance of LSIBs, including i) constructing a FLG anode with additional adsorption sites for the co-storage of Li-/Na-ions; ii) forming ND@Li/Na units as a new Li/Na storage platform in graphite matrix for improving the capacity during the charge-discharge processes; iii) creating LiF-/NaF-rich hybrid SEIs for enhancing the ionic mobility, mechanical strength, and reversibility; iv) experimentally achieving the theoretical maximum Li storage (LiC₆) in the graphite anode; v) theoretically simulating molecular dynamics of ND to open graphite layers and embed in graphite with Li-ions. This work provides a highly effective strategy to solve the problems of state-of-the-art LIBs with high cost/poor safety and SIBs with low capacity/lack of suitable anode material. The offered promising approach is greatly helpful for realizing industrial-scale production of secondary ion batteries with high performances and effectiveness.

4. Experimental Section

4.1. Preparation of Counter Electrode of Li-Na Alloy

In an argon-filled glove box, the thin foils (300 μm in thickness) of Li-Na alloys with varying mass ratios of Li and Na (1:1, 1:2, 1:5) were prepared by a mechanical compression method, as shown in Figure S1a. After multiple folding (six times)

and compressing processes, the color of alloy products changed gradually from gold to silvery, representing the full mixing of Li and Na metals with varying mass ratios of Li and Na (Figure S1b).

4.2. Preparation of Mixed Electrolytes and Pretreatment of Nanodiamonds (NDs)

The mixed electrolyte was obtained by mixing equal amounts of 1 mol L⁻¹ NaPF₆ and LiPF₆ in a solution of ethylene carbonate/dimethyl carbonate (by volume ratio of 1:1). The Functional ND powders (with an average diameter of 5 nm) were first pretreated in a vacuum chamber at 500 °C with flowing 50 sccm hydrogen gas (purified to 99.99%). The as-treated 0.005 g NDs powders were dispersed in 50 mL ethanol solution and intermittently ultrasound for 4 h, following a centrifuging process at 10 000 rpm for 5 min. In this paper, introducing ND in the cells was performed by dropping the dispersed ND colloidal suspension on the commercial polypropylene (PP) separators (DPP). The pre-hydrogenated NDs appearing with C-H stretching bands on the surface (Figure S1), which is beneficial to form ultra-dispersed colloid for LSIB modification, results in an enhanced electronegativity and wettability of electrolyte.^[38]

4.3. Preparation of Carbon-Coated Li_{1.5}Na_{1.5}V₂(PO₄)₃ (LNVP-C) Cathode

The three-dimensional (3D) interconnected porous Li_{1.5}Na_{1.5}V₂(PO₄)₃ (LNVP-C) was synthesized by a modified sol-gel method. Sodium hydroxide (NaOH), lithium hydroxide (LiOH), ammonium metavanadate (NH₄VO₃), ammonium dihydrogen phosphate (NH₄H₂PO₄), and citric acid monohydrate (C₆H₁₀O₈) were used as the precursors with a molar ratio of 3:3:4:6:4. The NH₄VO₃ and C₆H₁₀O₈ were firstly mixed with distilled water under magnetic stirring at 80 °C. When a bright blue solution was formed, NaOH, LiOH, and NH₄H₂PO₄ were added, in turn, with constant stirring at 80 °C for 10 h to obtain a blue homogeneous solution. The prepared solution was dried at 80 °C overnight, ground well and preheated at 350 °C for 4 h, followed by annealing at 750 °C for 8 h at a heating rate of 5 °C min⁻¹ in Ar atmosphere to obtain the 3D interconnected porous LNVP-C materials.

Assembly of the symmetric cells, half-cells and full-cells. The coin cells were assembled in an argon-filled glove box (the concentrations of residual O₂ and H₂O are <1 ppm). The electrodes were prepared by casting a mixture of active material, acetylene black, and poly(vinyl difluoride) (PVDF) binder in a weight ratio of 80:10:10 onto copper foils (graphite anode) and aluminum foils (LNVP-C cathode), followed by drying at 110 °C and 110 °C in vacuum for 12 h, respectively. The symmetric cells were assembled with two Li, Na, or Li/Na alloy slices as the counter electrodes, respectively. The LIB half-cells were assembled with metallic Li as the counter electrode, 1 M LiPF₆ in a mixture of ethylene carbonate/dimethyl carbonate (EC/DMC, 1:1 by volume) as the electrolyte (named as Li-ion electrolyte), and polypropylene (PP) as the separator. The SIBs were fabricated under the same conditions, except using sodium (Na) as a counter electrode and 1 M NaPF₆ in a mixture of ethylene carbonate/dimethyl carbonate (EC/DMC, 1:1 by volume) as the electrolyte (named as Na-ions electrolyte). The LSIBs were assembled as for LIBs and SIBs, except taking Li-Na alloys as the counter electrode instead of metallic Li or Na, and the sole Li-ion-, Na-ion-, or mixed Li-/Na-ion-electrolytes were performed in the cells for comparison. The LSIB full-cells were assembled by coupling the graphite anodes with LNVP cathodes at the weight ratio of 1:3.

4.4. Material Characterizations

The morphologies of graphite anode and LNVP-C cathode before and after cycling were characterized by scanning electron microscopy (SEM, FEI-magellan400, JEOL), transmission electron microscopy (TEM, JEM-2100F, JEOL) equipped with an energy-dispersive X-ray spectrometer (EDS), Raman spectroscopy (Witech CRM200, 532 nm), X-ray photoelectron spectroscopy (XPS,

ESCALAB-250Xi) and X-ray diffraction spectroscopy (XRD, 6000 AS-3K, NOPC). For *in-situ* XRD tests, a stainless-steel Swagelok-type battery with a Be window was assembled in the range of 0.01–3.00 V.

Received: November 27, 2023
Revised: January 30, 2024
Published online: February 21, 2024

4.5. Electrochemical Property Measurements

Electrochemical measurements of the second ion batteries were performed using two electrodes of CR2025 button cells. Constant current charge-discharge tests under a different current density were carried out on Land Batteries. Measurement System (CT2001 1A) with a cut-off voltage of 0.01–3.0 V for half-cells and 2.8–4.4 V for full-cells. Cyclic voltammograms (CVs) of scanning rate at 0.1 mV s⁻¹ and electrochemical impedance spectroscopy (EIS) were examined by CHI660E electrochemical workstation. Cycle performances, EIS, CVs, and rate capability tests were all carried out at room temperature. The galvanostatic intermittent titration technique (GITT) curves of graphite anode in LSIBs during a discharge-charge cycle as a function of time were tested with a discharge-charge rate of 0.1 C for an interval of 4 h, followed by an open circuit voltage for 40 min.

4.6. Methodological Details of Simulations

The dispersion-corrected density functional theory (DFT-D3)^[39] based on first principles calculation was used to simulate the experimental process of inserting ND in graphite anode. The structure optimization was performed at the Perdew-Burke-Ernzerh of (PBE)-D3 level with the Goedecker-Teter-Hutter (GTH)-DZVP basis sets.^[40] The box size was 50 Å × 50 Å × 50 Å to ensure at least 15 Å vacuum at x, y, and z directions to obtain a non-periodic system. An ND cluster consisting of 75 carbon atoms in cubic phase with surface reconstruction after structural optimization is selected to interact with the simplified graphite anode of bilayered graphene (TLG) with AA stacking configuration having lithiated LiC₆. In addition, hydrogenation on the outmost edge sides of the TLG is performed to keep the stability of the original structure. The molecular dynamics were implemented with NVT ensemble (atomic number N, volume V, and temperature T were kept constant). Geometric calculations were performed by the CP2K suite^[29] and electronic structures were analyzed by the Multiwfn 3.8 package.^[41]

The first principles calculation using a VASP code^[42] was performed to calculate the adsorption abilities of Li and Na on a diamond surface. The adsorption energies (E_{ads}) were obtained using the equation of $E_{\text{ads}} = (E_{\text{tot}} - E_{\text{sub}} - nE_{\text{atom}})/n$, where E_{tot} is the total energy for the diamond supercell with adsorbed Li or Na atoms, E_{sub} is the total energy of the pristine cell without adsorption, n is the number of adsorbed Li or Na atoms, and E_{atom} is the energy of a single Li or Na atom in a vacuum. In the calculations, the normal (111) and (100) facets of the diamond surface were reconstructed. The 2×2 supercells of diamond (111) and (100) surfaces were employed as the feasible adsorption sites for Li or Na atoms.

Acknowledgements

This work was supported by the National Natural Science Foundation of China (NSFC) (No. 52172044), Jilin Provincial Key Research and Development Plan Project (No. 20230201151 GX), the Engineering and Physical Sciences Research Council (EPSRC, EP/V027433/3).

Data availability statement

The data supporting the findings of this study are available within the article and its [Supporting Information](#) files.

Supporting Information

Supporting Information is available from the Wiley Online Library or from the author.

- [1] S. K. Hou, X. Ji, K. Gaskell, P. F. Wang, L. Wang, J. Xu, R. Sun, O. Borodin, C. S. Wang, *Science* **2021**, 374, 172.
- [2] C. L. Zhao, Q. D. Wang, Z. P. Yao, J. L. Wang, B. Sánchez-Lengeling, F. X. Ding, X. G. Qi, Y. X. Lu, X. D. Bai, B. H. Li, H. Li, M. Wagemaker, L. Chen, Y. S. Hu, *Science* **2020**, 370, 708.
- [3] M. Goktas, C. Bolli, E. J. Berg, P. Novák, K. Pollok, F. Langenhorst, M. V. Roeder, O. Lenchuk, D. Mollenhauer, P. Adelhelm, *Adv. Energy Mater.* **2018**, 8, 1702724.
- [4] V. Palomares, P. Serras, I. Villaluenga, K. B. Hueso, J. Carretero-González, T. Rojo, *Energ. Environ. Sci.* **2012**, 5, 5884.
- [5] X. Gao, H. Wu, C. Su, C. Lu, Y. Dai, S. Zhao, X. Hu, F. Zhao, W. Zhang, I. P. Parkin, C. J. Carmalt, G. He, *Energ. Environ. Sci.* **2023**, 16, 1364.
- [6] Y. Jin, P. M. L. Le, P. Gao, Y. Xu, B. Xiao, M. H. Engelhard, X. Cao, T. D. Vo, J. Hu, L. Zhong, B. E. Matthews, R. Yi, C. Wang, X. Li, J. Liu, J.-G. Zhang, *Nat. Energy* **2022**, 7, 718.
- [7] F. Xie, Z. Xu, A. C. S. Jensen, H. Au, Y. X. Lu, V. Araullo-Peters, A. J. Drew, Y. S. Hu, M. M. Titirici, *Adv. Funct. Mater.* **2019**, 29, 1901072.
- [8] Y. Li, Y. S. Hu, X. Qi, X. Rong, H. Li, X. Huang, L. Chen, *Energy Storage Mater.* **2016**, 5, 191.
- [9] J. L. Liu, Y. Q. Zhang, L. Zhang, F. X. Xie, A. Vasileff, S. Z. Qiao, *Adv. Mater.* **2019**, 31, 1901261.
- [10] D. Y. Yu, P. V. Prikhodchenko, C. W. Mason, S. K. Batabyal, J. Gun, S. Sladkevich, A. G. Medvedev, O. Lev, *Nat. Commun.* **2013**, 4, 2922.
- [11] J. Z. Guo, Y. Yang, D. S. Liu, X. L. Wu, B. H. Hou, W. L. Pang, K. C. Huang, J. P. Zhang, Z. M. Su, *Adv. Energy Mater.* **2018**, 8, 1702504.
- [12] Q. Zhang, Y. Lu, L. Miao, Q. Zhao, K. Xia, J. Liang, S. L. Chou, J. Chen, *Angew. Chem. Int. Ed.* **2018**, 57, 14796.
- [13] H. X. Wang, Y. Cui, *Carbon Energy* **2019**, 1, 13.
- [14] X. Zhai, J. Feng, X. Sun, C. Wang, X. Zhang, Z. Cui, J. Liu, H. Li, *J. Alloys Compd.* **2023**, 933, 167621.
- [15] C. Wang, X. Sun, J. Zhang, X. Zhai, X. Zhang, Z. Li, H. Li, *Chem. Eng. J.* **2023**, 466, 143191.
- [16] H. S. Hirsh, Y. Li, D. H. S. Tan, M. Zhang, E. Zhao, Y. S. Meng, *Adv. Energy Mater.* **2020**, 10, 2001274.
- [17] C. Scordilis-Kelley, R. T. Carlin, *J. Electrochem. Soc.* **1993**, 140, 1606.
- [18] Y. P. Song, H. D. Li, L. Y. Wang, D. C. Qiu, Y. B. Ma, K. Pei, G. T. Zou, K. F. Yu, *Chem. Commun.* **2016**, 52, 10497.
- [19] J. L. Ma, F. L. Meng, Y. Yu, D. P. Liu, J. M. Yan, Y. Zhang, X. B. Zhang, Q. Jiang, *Nat. Chem.* **2019**, 11, 64.
- [20] X. Gao, Y. Dai, C. Zhang, Y. Zhang, W. Zong, W. Zhang, R. Chen, J. Zhu, X. Hu, M. Wang, R. Chen, Z. Du, F. Guo, H. Dong, Y. Liu, H. He, S. Zhao, F. Zhao, J. Li, I. P. Parkin, C. J. Carmalt, G. He, *Angew. Chem. Int. Ed.* **2023**, 62, e202300608.
- [21] M. Song, Z. Yi, R. Xu, J. Chen, J. Cheng, Z. Wang, Q. Liu, Q. Guo, L. Xie, C. Chen, *Energy Storage Mater.* **2022**, 51, 620.
- [22] Z. Yuan, L. Wang, D. Li, J. Cao, W. Han, *ACS Nano* **2021**, 15, 7439.
- [23] X. B. Cheng, M. Q. Zhao, C. Chen, A. Pentecost, K. Maleski, T. Mathis, X. Q. Zhang, Q. Zhang, J. Jiang, Y. Gogotsi, *Nat. Commun.* **2017**, 8, 336.
- [24] S. T. Weng, S. Y. Wu, Z. P. Liu, G. J. Yang, X. Liu, X. Zhang, C. Zhang, Q. Y. Liu, Y. Huang, Y. J. Li, M. N. Ateş, D. Su, L. Gu, H. Li, L. Q. Chen, R. J. Xiao, Z. X. Wang, X. F. Wang, *Carbon Energy* **2022**, DOI: 10.1002/cey2.224.
- [25] H. Kim, J. Hong, Y. U. Park, J. Kim, I. Hwang, K. Kang, *Adv. Funct. Mater.* **2015**, 25, 534.
- [26] P. Luo, C. Zheng, J. He, X. Tu, W. P. Sun, H. Pan, Y. P. Zhou, X. H. Rui, B. Zhang, K. Huang, *Adv. Funct. Mater.* **2021**, 32, 2107277.
- [27] T. Zhang, W. He, W. Zhang, T. Wang, P. Li, Z. Sun, X. Yu, *Chem. Sci.* **2020**, 11, 8686.

- [28] Y. Deng, J. Zheng, Q. Zhao, J. Yin, P. Biswal, Y. Hibi, S. Jin, L. A. Archer, *Small* **2022**, *18*, 2203409.
- [29] J. Hutter, M. Iannuzzi, F. Schiffmann, J. VandeVondele, *WIREs Comput. Mol. Sci.* **2014**, *4*, 15.
- [30] K. P. C. Yao, J. S. Okasinski, K. Kalaga, I. A. Shkrob, D. P. Abraham, *Energy Environ. Sci.* **2019**, *12*, 656.
- [31] Q. Liu, R. Xu, D. Mu, G. Tan, H. Gao, N. Li, R. Chen, F. Wu, *Carbon Energy* **2022**, DOI: [10.1002/cey2.120](https://doi.org/10.1002/cey2.120).
- [32] X. Wu, B. Song, P. H. Chien, S. M. Everett, K. Zhao, J. Liu, Z. Du, *Adv. Sci.* **2021**, *8*, 2102318.
- [33] Z. L. Jian, Z. Y. Xing, C. Bommier, Z. F. Li, X. L. Ji, *Adv. Energy Mater.* **2016**, *6*, 1501874.
- [34] Y. J. Mai, D. Zhang, Y. Q. Qiao, C. D. Gu, X. L. Wang, J. P. Tu, *J. Power Sources* **2012**, *216*, 201.
- [35] Y. Wang, F. Liu, G. Fan, X. Qiu, J. Liu, Z. Yan, K. Zhang, F. Cheng, J. Chen, *J. Am. Chem. Soc.* **2021**, *143*, 2829.
- [36] F. A. Soto, P. Yan, M. H. Engelhard, A. Marzouk, C. Wang, G. Xu, Z. Chen, K. Amine, J. Liu, V. L. Sprenkle, F. El-Mellouhi, P. B. Balbuena, X. Li, *Adv. Mater.* **2017**, *29*, 1606860.
- [37] Y. P. Wu, X. K. Huang, L. Huang, J. H. Chen, *Energy Environ. Mater.* **2020**, *4*, 19.
- [38] H. A. Girard, T. Petit, S. Perruchas, T. Gacoin, C. Gesset, J. C. Arnault, P. Bergonzo, *Phys. Chem. Chem. Phys.* **2011**, *13*, 11517.
- [39] Y. S. Lin, G. D. Li, S. P. Mao, J. D. Chai, *J. Chem. Theory Comput.* **2013**, *9*, 263.
- [40] H. Zhang, Y. Yang, D. Ren, L. Wang, X. He, *Energy Storage Mater.* **2021**, *36*, 147.
- [41] T. Lu, F. Chen, *J. Comput. Chem.* **2012**, *33*, 580.
- [42] J. Y. Jiao, R. J. Xiao, M. Tian, Z. X. Wang, H. P. Chen, *Electrochimica Acta* **2018**, *282*, 205.